


Effects of Subgrid Terrain Radiative Forcing on the Ability of RegCM4.1 in the Simulation of Summer Precipitation Over China

Chunlei Gu^{1,2}, Anning Huang¹ , Yang Wu¹, Ben Yang¹, Xiyu Mu^{3,4} , Xindan Zhang¹, and Shuxin Cai¹

¹CMA-NJU Joint Laboratory for Climate Prediction Studies and State Key Laboratory of Severe Weather and Joint Center for Atmospheric Radar Research of CMA/NJU, School of Atmospheric Sciences, Nanjing University, Nanjing, China, ²Lianyungang Meteorological Bureau, Lianyungang, China, ³Key Laboratory of Transportation Meteorology, China Meteorological Administration, Nanjing, China, ⁴Jiangsu Institute of Meteorological Sciences, Nanjing, China

Key Points:

- A subgrid terrain radiative forcing (STRF) scheme was developed
- RegCM4.1 model with considering the STRF effect improved the summer precipitation simulation over China

Correspondence to:

A. Huang,
 anhuang@nju.edu.cn

Citation:

Gu, C., Huang, A., Wu, Y., Yang, B., Mu, X., Zhang, X., & Cai, S. (2020). Effects of subgrid terrain radiative forcing on the ability of RegCM4.1 in the simulation of summer precipitation over China. *Journal of Geophysical Research: Atmospheres*, 125, e2019JD032215. <https://doi.org/10.1029/2019JD032215>

Received 9 DEC 2019

Accepted 30 APR 2020

Accepted article online 9 MAY 2020

Author Contributions:

Data curation: Chunlei Gu, Yang Wu, Xiyu Mu, Shuxin Cai

Formal analysis: Chunlei Gu

Investigation: Xindan Zhang

Methodology: Chunlei Gu

Resources: Ben Yang

Software: Chunlei Gu

Validation: Chunlei Gu

Visualization: Chunlei Gu, Yang Wu, Xiyu Mu

Writing - original draft: Chunlei Gu

Writing - review & editing: Yang Wu, Ben Yang

Abstract We implemented a subgrid terrain radiative forcing (STRF) scheme into the International Centre for Theoretical Physics, Italy, Regional Climate Model Version 4.1 (RegCM4.1) and evaluated its impacts on the summer precipitation simulation over China by comparing the model results from the experiments with and without the STRF scheme. The RegCM4.1 without the STRF scheme simulates strong East Asian summer monsoon and overestimates the summer precipitation over China. Adopting the STRF scheme in the RegCM4.1 improves the representation of surface radiation process over complex terrains, by reducing the net gain of the surface radiation energy over the Tibetan Plateau (TP). As a result, the heat released from the surface to the overlying air column decreases, thus suppressing the development of local convection over the TP. In addition, the weakened TP thermal forcing due to the STRF effect reduces the land-sea thermal contrast, resulting in a weakened East Asian summer monsoon that produces less transport of water vapor from tropical oceans and hence weakens summer precipitation over China. Our analysis indicates that such improvement in the precipitation simulation induced by the STRF effect is mainly due to the improved simulation of precipitation intensity, particularly that associated with the moderate and heavy precipitation events, and convective processes.

1. Introduction

The differential heating of the planet through solar energy (Vardavas & Taylor, 2011) primarily drives the Earth's climate system. The Earth surface can absorb about half of the incident solar radiation and then emit the long-wave radiation that effectively heats the atmosphere (Stocker, 2014). The balance between the incoming energy and outgoing energy determines the mean state of climate (Solomon et al., 2007), and any perturbation in such balance can influence the climate (Vardavas & Taylor, 2011). Therefore, the balance of radiative forcing is crucial for the normal maintenance of the climate system.

Spatial surface heterogeneities significantly modify the radiation fluxes on the Earth's surface (Müller & Scherer, 2005). The slope, aspect, shadow, and obstruction of the topography highly influence the solar radiation on the land surface and have influence on the energy budget particularly over the areas with complex terrain (Essery & Marks, 2007; Whiteman et al., 1989). The influences of orographic heterogeneity in the subscale grids on the surface long-wave radiation flux over a large-scale grid area are important in the climate simulation (Zhang, Ding, & Chen, 2006). Numerous previous studies have investigated the effects of topographic thermal forcing on the surface radiation budget over complex terrains by adopting different computational methods for surface radiation fluxes (e.g., Chen, Zhang, & Ding, 2006; Dozier & Outcalt, 1979; Dubayah et al., 1990; Fu, 1958; Garnier & Ohmura, 1968; Li et al., 1996; Li & Weng, 1987; Wang et al., 2004; Zhang, Ding, & Chen, 2006).

Previous studies have indicated that increase in the horizontal resolution in the climate models can realistically resolve topographic influences on climate processes (e.g., Jain et al., 2019; Xu et al., 2018). To this end, a number of studies demonstrate the added value of regional climate models (RCMs) particularly in the spatial and temporal distribution of precipitation over complex terrain (Feser et al., 2011; Giorgi et al., 2009; Torma et al., 2015). RCMs have significantly improved the representation of the East Asian summer monsoon (EASM) over the years. However, a number of deficiencies in the representation of physical processes

©2020. The Authors.

This is an open access article under the terms of the Creative Commons Attribution License, which permits use, distribution and reproduction in any medium, provided the original work is properly cited.

remain unresolved (Fu et al., 2005; Qian & Leung, 2007; Yhang & Hong, 2008; Zou & Zhou, 2011). The International Centre of Theoretical Physics (ICTP) Regional Climate Model (RegCM, <http://gforge.ictp.it/gf/project/regcm/>) is one of the most widely used RCMs across the world (Elguindi et al., 2011; Giorgi et al., 2006). However, similar to other RCMs or GCMs, RegCM also exhibits limitations in modeling the precipitation over East Asia, especially in summer (Liu et al., 2013; Wu et al., 2015; Yu & Xie, 2013).

Increasing the model resolution enhances the impact of subgrid-scale orographic heterogeneities on the surface radiation fluxes (Hauge & Hole, 2003; Müller & Scherer, 2005; Zhang, Ding, & Chen, 2006), particularly over the complex terrain such as the Tibetan Plateau (TP) (Liou et al., 2007). Therefore, several subgrid-scale terrain radiative forcing (STRF) schemes have been developed and tested in different numerical models (e.g., Chen, Hall, & Liou, 2006; Gu et al., 2012; Hauge & Hole, 2003; Lee et al., 2011, 2015; Müller & Scherer, 2005; Ruiz-Arias et al., 2011; Senkova et al., 2007; Shen & Hu, 2006; Zhang, Huang, & Zhu, 2006). The use of STRF scheme improves the representation of the surface radiative processes and the energy budgets over the complex terrains, leading to better model performance in simulating the surface variables, that is, temperature, precipitation, and wind.

The TP is located in East Asia and covers an area of 2.5 million km² with mean elevation over 4,000 m. It has the most complex topography surrounded by the highest mountains in the world, such as the Himalayas, Pamir, Kunlun Shan, Hengduan Mountains, and Kailas Range, (Chen et al., 2003; Wu et al., 2007; Yang, Guo, He et al., 2011). It is widely considered that the TP has significant mechanical and thermal forcing influences on the climate around the globe. Many earlier studies suggest that the TP is a strong heat source for the middle tropospheric atmosphere during summer in the Northern Hemisphere (Flohn, 1957; Kitoh, 2004; Li et al., 2001; Li & Yanai, 1996; Liu et al., 2012; Moore, 2012; Yanai & Wu, 2006; Yeh et al., 1957), which can exert strong impacts on the evolution of the EASM system (Boo et al., 2011; Chang et al., 2013; Chen et al., 2010; Chiang et al., 2016; Kosaka et al., 2011; Xu & Xu, 2012; Yang et al., 2015; Zou et al., 2010).

In this study, we have incorporated the STRF scheme in the RegCM Version 4.1 (hereafter RegCM4.1) to more realistically represent surface radiation process over the regions with complex terrains, such as in East Asia. The impacts of STRF on the model's ability in simulating the summer precipitation over China and associated underlying mechanism are evaluated and discussed with the emphasis on the following questions addressed: (1) Can the STRF effect considered in the RegCM4.1 improve the model's ability in simulating the summer precipitation over China? (2) What are the physical drivers of precipitation differences between simulations with and without the STRF scheme?

The RegCM4.1, STRF scheme, numerical experiment design, data sets and analysis methods are described in section 2. Systematic evaluations of the effects of STRF on the model performance in summer precipitation simulation are presented in section 3. Section 4 explores the potential underlying mechanisms associated with the STRF effect on the simulated precipitation. The concluding remarks and summary are presented in section 5.

2. Model and Methodology

2.1. Model Description

The RegCM4.1 released by ICTP in May 2011 is a compressible, hydrostatic, and limited-area model using Arakawa B-grid and σ - p coordinate. Compared to the RegCM3, some modifications have been applied in the RegCM4.1, such as a better method of radiative cloud calculation, addition of the contribution from infrared spectrum to the aerosol radiative transfer calculation, and a new "mixed" cumulus convective scheme, etc. (Elguindi et al., 2011).

2.2. The STRF Parameterization Scheme

The terrain slope and aspect can reflect the microcharacteristics of topography. The terrain slope is defined as the angle between the horizontal plane and the inclined plane and ranges between 0° to 90°. The terrain aspect is the angle between the projection of the slope normal vector on the horizontal plane and the south direction clockwise (90° is west, 180° is north, 270° is east, and 0° or 360° is south). The terrain slope and aspect, referred respectively as α and β (Zhang, Huang, & Zhu, 2006), can be calculated by the gradient of the altitude H in the horizontal direction using the following mathematical expressions (Li & Weng, 1987):

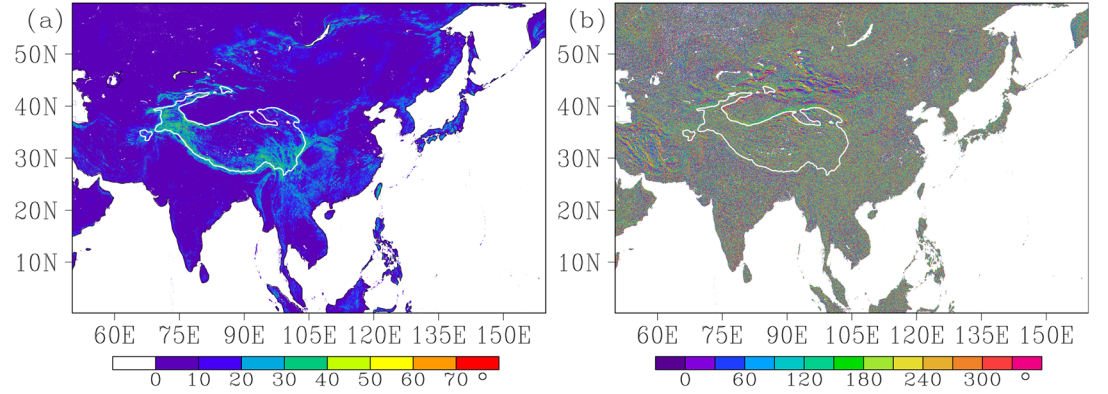


Figure 1. The terrain slope (a) and aspect (b) over East Asia with a horizontal resolution of 3 arc sec. The gray line marks the elevation of 3,000 m.

$$\alpha = \arctg \left[\left(\frac{\partial H}{\partial x} \right)^2 + \left(\frac{\partial H}{\partial y} \right)^2 \right]^{1/2} \quad (1)$$

$$\beta = \begin{cases} \frac{3\pi}{2} - \arctg \left(\frac{\partial H}{\partial y} / \frac{\partial H}{\partial x} \right), & \text{when } \frac{\partial H}{\partial x} < 0 \\ \frac{\pi}{2} - \arctg \left(\frac{\partial H}{\partial y} / \frac{\partial H}{\partial x} \right), & \text{when } \frac{\partial H}{\partial x} > 0 \end{cases} \quad (2)$$

The elevation of the model grid is derived from GTOPO30 data set (available at <https://lta.cr.usgs.gov/GTOPO30>) with a resolution of 30 arc sec (~1 km). The STRF parameterization is instead based on the Shuttle Radar Topography Mission (SRTM) global data set (Jarvis et al., 2008, available at <http://srtm.csi.cgiar.org>) with a resolution of 3 arc sec (~90 m), which ensures that the subgrid terrain in the RegCM4.1 can be well represented. The terrain slope and aspect derived from the SRTM data with a resolution of 3 arc sec are shown in Figure 1. The slope and aspect show highly detailed heterogeneity of the terrain over East Asia. The sharp slope with the maximum over 70° is mainly over the western, southern, and eastern TP flank.

The surface solar radiation flux (Fu, 1983; Weng et al., 1981) and long-wave radiation flux (Weng et al., 1981) over the inclined plane can be calculated by the following mathematical expressions:

$$S_{\alpha\beta} = I_0(u \sin \delta + v \cos \delta \cos \omega + w \cos \delta \sin \omega) \quad (3)$$

$$\begin{cases} u = \sin \varphi \cos \alpha - \cos \varphi \sin \alpha \cos \beta \\ v = \cos \varphi \cos \alpha + \sin \varphi \sin \alpha \cos \beta \\ w = \sin \beta \sin \alpha \end{cases} \quad (4)$$

$$F_{\alpha\beta} = F_0 \cos^2(\alpha/2) \quad (5)$$

where δ , ω , φ , I_0 , $S_{\alpha\beta}$, F_0 , and $F_{\alpha\beta}$ are the solar declination, time angle, latitude, solar constant, slope surface solar radiation flux, flat surface long-wave radiation flux, and slope surface long-wave radiation flux, respectively. The α and β are the terrain slope and aspect and can be calculated according to the equations 1 and 2. The units of δ , ω , φ , α , and β are radians. The units of I_0 , $S_{\alpha\beta}$, F_0 , and $F_{\alpha\beta}$ are W m^{-2} .

We assume the SRTM grid as the subgrid of the model grid. The surface solar radiation fluxes on each subgrid (marked as i), calculated by the mathematical expressions 3 and 4, can be interpolated onto the model grid (marked as p) with the inverse distance weighting method (Bartier & Keller, 1996):

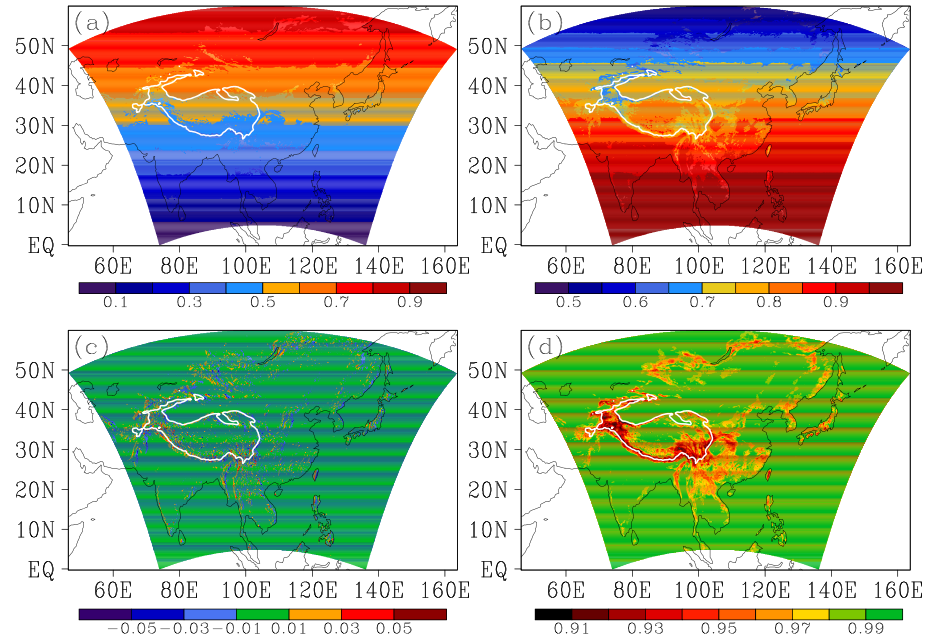


Figure 2. Calibration factors (a) \bar{u} , (b) \bar{v} , (c) \bar{w} , and (d) $\overline{\cos^2(\alpha/2)}$ on the model grids with a resolution of 20 km. The gray line marks the elevation of 3,000 m.

$$S_{\alpha\beta_p} = \frac{\sum_{i=1}^n \frac{S_{\alpha\beta_i}}{d_i}}{\sum_{i=1}^n \frac{1}{d_i}} = \sum_{i=1}^n \frac{I_0(u_i \sin \delta + v_i \cos \delta \cos \omega_i + w_i \cos \delta \sin \omega_i)}{d_i} / \sum_{i=1}^n \frac{1}{d_i} \quad (6)$$

where d_i is the horizontal distance from the i th subgrid to the center of its mother grid p . The solar declination δ and solar constant I_0 are independent of the spatial position of the grid or subgrid. The subgrid time angle ω_i is a neighborhood of the model grid time angle ω_p . Expand $\sin \omega_i$ and $\cos \omega_i$ to Taylor series:

$$\sin \omega_i = \sin \omega_p + (\omega_i - \omega_p) \cos \omega_p + \dots + o[(\omega_i - \omega_p)^n] \quad (7)$$

$$\cos \omega_i = \cos \omega_p - (\omega_i - \omega_p) \sin \omega_p + \dots + o[(\omega_i - \omega_p)^n] \quad (8)$$

The dimension of $\omega_i - \omega_p$ is 10^{-3} ; we can get the $\sin \omega_i \doteq \sin \omega_p$ and $\cos \omega_i \doteq \cos \omega_p$ by taking the zeroth-order approximation of $\omega_i - \omega_p$. Equation 6 can be rewritten as

$$S_{\alpha\beta_p} \doteq I_0 (\bar{u} \sin \delta + \bar{v} \cos \sigma \cos \omega_p + \bar{w} \cos \sigma \sin \omega_p) \quad (9)$$

Similarly, the surface long-wave radiation flux over the complex terrain areas is given by

$$F_{\alpha\beta_p} \doteq F_{0_p} \overline{\cos^2(\alpha/2)} \quad (10)$$

According to the equations 9 and 10, we can implement the STRF scheme in the RegCM4.1 in two steps. First, we precalculate u_i , v_i , w_i , and $\cos^2(\alpha_i/2)$ on each subgrid (SRTM grid) i and then we interpolate them onto the model grid p to get the calibration factors \bar{u} , \bar{v} , \bar{w} , and $\overline{\cos^2(\alpha/2)}$ before the model time integration starts. Second, we calibrate the surface solar and long-wave radiation fluxes with \bar{u} , \bar{v} , \bar{w} , and $\overline{\cos^2(\alpha/2)}$ during the model time integration when the atmosphere-surface interaction takes place (Gu et al., 2018).

Figure 2 gives the surface radiative forcing calibration factors \bar{u} , \bar{v} , \bar{w} , and $\overline{\cos^2(\alpha/2)}$ on each model grid in the model domain. The \bar{u} and \bar{v} are dependent of the latitude, terrain slope, and aspect. The \bar{u} (\bar{v}) increases (decreases) over the flat area as the latitude increases. The \bar{u} and \bar{v} over the complex terrain are smaller than those over the flat areas in the same latitudes. Both \bar{w} and $\overline{\cos^2(\alpha/2)}$ are highly subject to the slope and

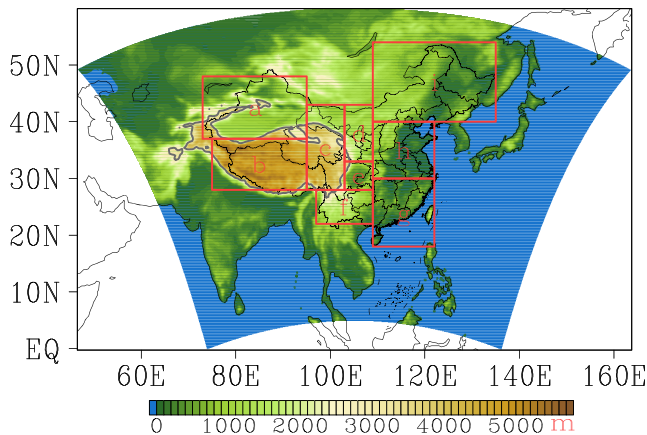


Figure 3. The surface elevation on each model grid in the model domain. The nine subregions are denoted by red rectangles (a = Reg1, b = Reg2, c = Reg3, d = Reg4, e = Reg5, f = Reg7, g = Reg7, h = Reg8, and i = Reg9). The gray line marks the elevation of 3,000 m.

become important for radiation simulations over the heterogeneous regions with sharp slope, such as the TP and Tianshan Mountain.

2.3. Numerical Experiment Design

We conduct two model experiments, one without the STRF scheme (hereafter CTRL) and the other with the STRF scheme (hereafter SEXP). The RegCM4.1 is configured using 18 vertical levels with its top at 50 hPa. Following Chen et al. (2014), the model domain consists of 405×315 grid points with the grid spacing at 20 km and its center at 105°E , 32°N , covering most parts of East Asia and its adjacent regions (Figure 3). The model employs the Grell convection scheme (Grell, 1993) that uses the Fritsch and Chappell closure (Fritsch & Chappell, 1980). The land surface processes are represented by the Biosphere-Atmosphere Transfer scheme (Dickinson et al., 1993) without subgridding. Other model physical schemes include the Zeng ocean flux scheme (Zeng et al., 1998), subgrid explicit moisture scheme (SUBEX, Pal et al., 2000), and the Holtslag planetary boundary layer scheme (Holtslag et al., 1990). The relaxation of exponential technique is adopted for the lateral boundary conditions with a lateral buffer zone of 12 grids width.

The model integration for each experiment is carried out from 1 May to 31 August in each year during 2007–2012. The time steps for the radiation model, long-wave radiation absorption/emissivity process, land surface model, and atmosphere model are 10 min, 6 min, 90 s, and 30 s, respectively. The model outputs are archived at daily frequency. We discard the first month as spin-up time following Zhong et al. (2007), Kang et al. (2014), and Gao et al. (2016) and utilize the model outputs from 1 June to 31 August for analysis.

The model setup (i.e., the small number of vertical levels, relatively short spin-up time, small lateral buffer zone, and low-resolution driving fields) might cause certain systematic errors. Nevertheless, we focus on the simulation differences between the SEXP and CTRL experiments, which should largely remove these systematic errors. However, we highly recommend finer vertical resolution, longer spin-up time, larger lateral buffer zone, and high-resolution driving fields for better model performance potentially.

2.4. Data and Methodology

The initial and lateral boundary conditions of the RegCM4.1 are derived from the 6-hourly National Centers for Atmospheric Prediction/National Center for Atmospheric Research (NCEP/NCAR) reanalysis data with a horizontal resolution of $2.5^\circ \times 2.5^\circ$ at 17 vertical levels (Kalnay et al., 1996), which are available at the website (<https://www.esrl.noaa.gov/psd/data/gridded/data.ncep.reanalysis.html>). The NOAA weekly OISST data with a horizontal resolution of $1.0^\circ \times 1.0^\circ$ (Reynolds et al., 2008) provides the oceanic boundary conditions of the RegCM4.1, and the data are available online (<https://www.esrl.noaa.gov/psd/data/gridded/data.noaa.oisst.v2.html>).

Additionally, the following data are used for model evaluation: (1) The daily observed grid precipitation data set with a horizontal resolution of $0.25^\circ \times 0.25^\circ$ over monsoon Asia (APHRO_MA_V1101EX_R1, Yatagai et al., 2012, available at <http://aphrodite.st.hirosaki-u.ac.jp>). (2) The monthly total and convective precipitation fields, wind fields, and humidity fields derived from the ERA-interim reanalysis data sets with a horizontal resolution of $0.75^\circ \times 0.75^\circ$ (Dee et al., 2011, available at <https://www.ecmwf.int>). The ERA-interim data sets have high skills in the EASM precipitation simulation relative to other reanalysis data sets and share the general features of summer rainfall with the APHRO data (Huang et al., 2016; Lin et al., 2014). Although the ERA-interim convective precipitation may have uncertainties, it still can be utilized as a reference in the model evaluation (Kang et al., 2014).

The simulated data are interpolated onto the $0.25^\circ \times 0.25^\circ$ APHRO grid and $0.75^\circ \times 0.75^\circ$ ERA-interim grid using the area-weighted average method (referred to the details at <http://www.opengrads.org/doc/udxt/re/>). The precipitation simulations are mainly evaluated with the APHRO data except that the biases in Figure 8 are based on the ERA-interim data. Following Pierce et al. (2013) and Caldwell et al. (2009), the rainy days are defined as days with daily precipitation over 0.1 mm from 1 June to 31 August in each year during

2007–2012 (552 days). The summer mean precipitation frequency (PF, the number of rainy days divided by 552), precipitation amount (PA, the accumulated precipitation of rainy days divided by 552), and precipitation intensity (PI = PA/PF) are calculated according to Zhou et al. (2008) and Kan et al. (2015).

We assess the impact of the STRF on the model performance over nine different subregions of China (see Figure 3), which are defined based on the annual mean precipitation distribution, mountain ranges, elevations, and climate zones (Ding & Chan, 2005; Gao et al., 2006). The nine subregions are Reg1-Xinjiang (37–48°N, 73–97°E), Reg2-central and western TP (28–37°N, 75–95°E), Reg3-eastern TP (28–43°N, 95–103°E), Reg4-upper reaches of the Yellow River valley (33–43°N, 103–109°E), Reg5-Sichuan Basin (28–33°N, 103–109°E), Reg6-Yungui Plateau (22–28°N, 97–109°E), Reg7-southeastern China (18–30°N, 109–122°E), Reg8-northern China-Jianghuai Basin (30–40°N; 109–122°E), and Reg9-northeastern China (40–54°N, 109–135°E) (Huang et al., 2016).

Following Kan et al. (2015) and Huang, Zhao et al. (2016), we use the Taylor score (TS) (Taylor, 2001) and relative error (RE) for the evaluations of precipitation simulation, with higher (lower) TS (absolute value of RE) indicates better model performance.

$$TS = \frac{4(1 + PC)}{(\gamma + 1/\gamma)^2(1 + PC_0)} \quad (11)$$

$$\gamma = \sqrt{\frac{1}{n} \sum_{i=1}^n (M_i - \bar{M})^2} / \sqrt{\frac{1}{n} \sum_{i=1}^n (O_i - \bar{O})^2} \quad (12)$$

$$PC = \sqrt{\sum_{i=1}^n (O_i - \bar{O})(M_i - \bar{M})} / \sqrt{\sum_{i=1}^n (O_i - \bar{O})^2 \sum_{i=1}^n (M_i - \bar{M})^2} \quad (13)$$

$$RE = \frac{M - O}{O} \times 100\% \quad (14)$$

where M and O represent the simulated and observed variables, respectively. The γ is the ratio between the simulated and the observed spatial standard deviation, which represents the agreements of the spatial variability between the simulations and the observations. PC is the spatial correlation coefficient between the simulated and the observed fields, and its maximum value PC_0 is usually set to 1.

3. Model Evaluation

The summer mean precipitation amount, frequency, and intensity over China from the observation and the two experiments are shown in Figure 4. Overall, the general characteristics of PA, PF, and PI over China in summer are well captured by the RegCM4.1, but some model biases still exist in reproducing the distribution of the maximum center of PA, PI, and PF. Meanwhile, there are obvious differences between the CTRL and SEXP experiments, especially in the PA and PI. As shown in Figures 4a–4c, both the CTRL and SEXP experiments reproduce the northwestward decreasing trend of the summer PA. However, the simulated maximum PA in the CTRL experiment is located over the northern China and the southeastern TP rather than over the southeastern regions as in the observations. The RegCM4.1 with the STRF scheme obviously reduces the positive biases of PA over the southeastern TP and the North China Plain. Figures 4d–4f show that the CTRL experiment reproduces the high-low-high PF distribution from south to north but with errors in the lower reaches of the Yellow River and the middle to lower reaches of the Yangtze River. Figures 4g–4i reveal that the CTRL experiment generates the general northwestward decreasing trend of PI but with the underestimation in the southeastern China and the overestimation over the rest of China.

To reveal the differences between the observations and the simulations, the summer mean PA, PF, and PI differences between the CTRL experiment and the observations (Figures 5a–5c), those between the SEXP experiment and the observations (Figures 5d–5f), and those between the two experiments (Figures 5g–5i) are presented. The PA and PI differences show similar spatial distribution. The CTRL experiment overestimates the PA and PI in most regions of Mainland China except the southeast coast and northwest arid area with the largest positive biases of PA and PI located in the southeastern TP flank. Adopting the STRF scheme in the RegCM4.1 reduces the positive biases of PA and PI in the southern and eastern TP, Yungui Plateau,

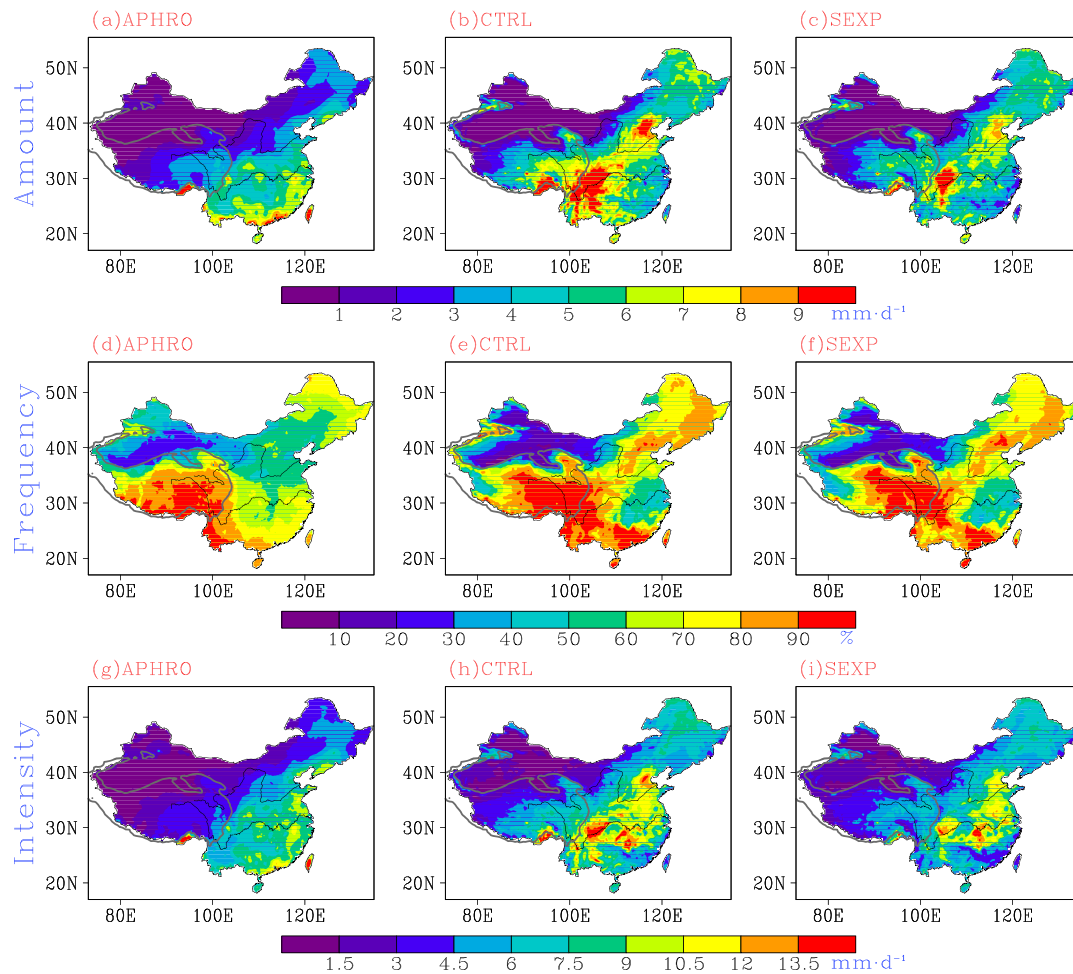


Figure 4. (a–i) Spatial distributions of the observed and simulated summer mean PA, PF, and PI averaged over 2007 – 2012. The gray line marks the elevation of 3,000 m. The Yangtze River and Yellow River are indicated by the dark curve lines.

Sichuan Basin, and northeastern China but increases the negative biases of PA and PI in the southeastern China.

As shown in Figures 5b, 5e, and 5h, the CTRL experiment produces negative biases of PF in the downstream reaches of Yangtze River, southwestern TP, most area of Xinjiang except Tianshan, and part of the inner Mongolia Plateau and the positive biases of PF in the rest region of Mainland China. The largest negative biases are located in the western TP, the Junggar Basin, and the Tarim Basin, while the largest positive biases are located in northern China. With the STRF scheme, the simulated biases of PF are slightly narrowed in part of the eastern TP, northern TP, northwestern China, and southern China but expanded in northern China.

We have preliminarily analyzed the simulated precipitation differences between the two experiments above. Figure 6 shows these differences in each subregion in term of TS and RE of the simulated PA, PF, and PI. As shown in Figures 6a and 6d, the SEXP experiment produces higher TS and lower absolute value of RE for PA in most subregions except Reg7, indicating that the STRF scheme improves the summer PA simulation over most of China except southeastern China. The improvements are most obvious over the eastern TP (Reg3) with an increase of 0.23 in TS and 35% decrease in RE. Although the RE for PA, respectively, decreases by 24%, 38%, and 16% in Reg2, Reg5, and Reg8, the TS for PA simulation in these subregions is not obviously increased due to the decreased spatial correlation coefficient of PA (not shown).

Figures 6b and 6e show that the simulated PF over China is not quite sensitive to the STRF scheme. Figures 6c and 6f reveal that the higher (lower) values of TS (absolute RE) for PI over most of China are

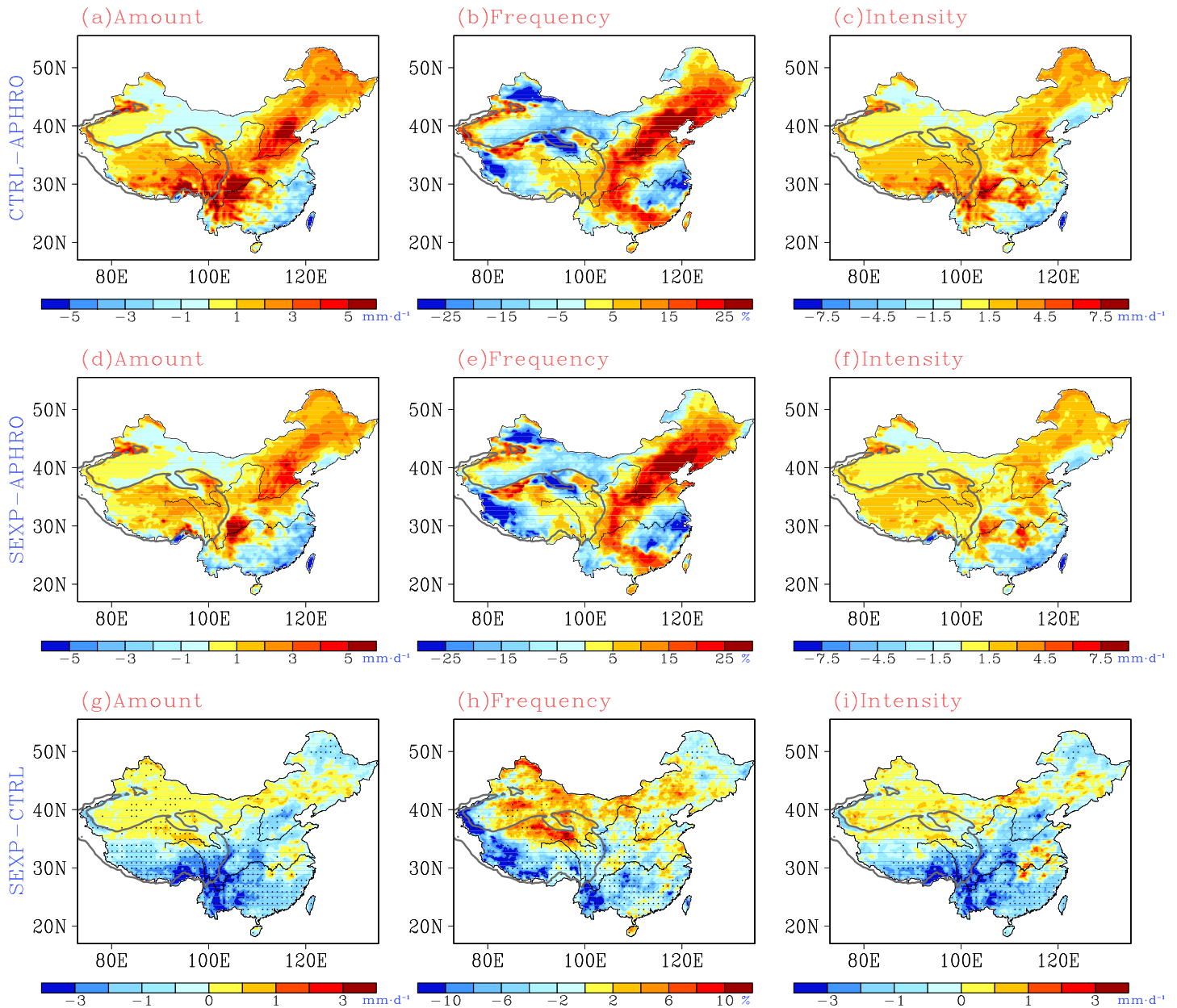


Figure 5. The spatial distributions of the differences between CTRL and APHRO (CTRL – APHRO, a–c), between SEXP and APHRO (SEXP – APHRO, d–f), and between CTRL and SEXP (SEXP – CTRL, g–i) in the summer mean PA, PF, and PI averaged over 2007 – 2012, respectively. Dots indicate the differences that are significant at 95% confidence level. The gray line marks the elevation of 3,000 m. The Yangtze River and Yellow River are indicated by the dark curve lines.

obtained by the RegCM4.1 with the STRF scheme. The largest PI improvement also occurs in the eastern TP (Reg3) with the TS increased by 0.22 and the RE decreased by 27%. Overall, the summer precipitation simulations over most of China are improved due to the adoption of the STRF scheme. The better simulated PA are mainly due to the improvements in the PI rather than the PF.

To further understand the sources of the simulated regional precipitation biases, we compare the PA differences between the simulations and the observations for the different precipitation categories classified based on the daily precipitation (Figure 7) or convective/nonconvective precipitation (Figure 8).

Following Qiao et al. (2012), we classify the daily precipitation into light, moderate, heavy, and torrential precipitation with the thresholds of 0.1–9.9, 10–24.9, 25–49.9, and ≥ 50 mm-day⁻¹, respectively. The

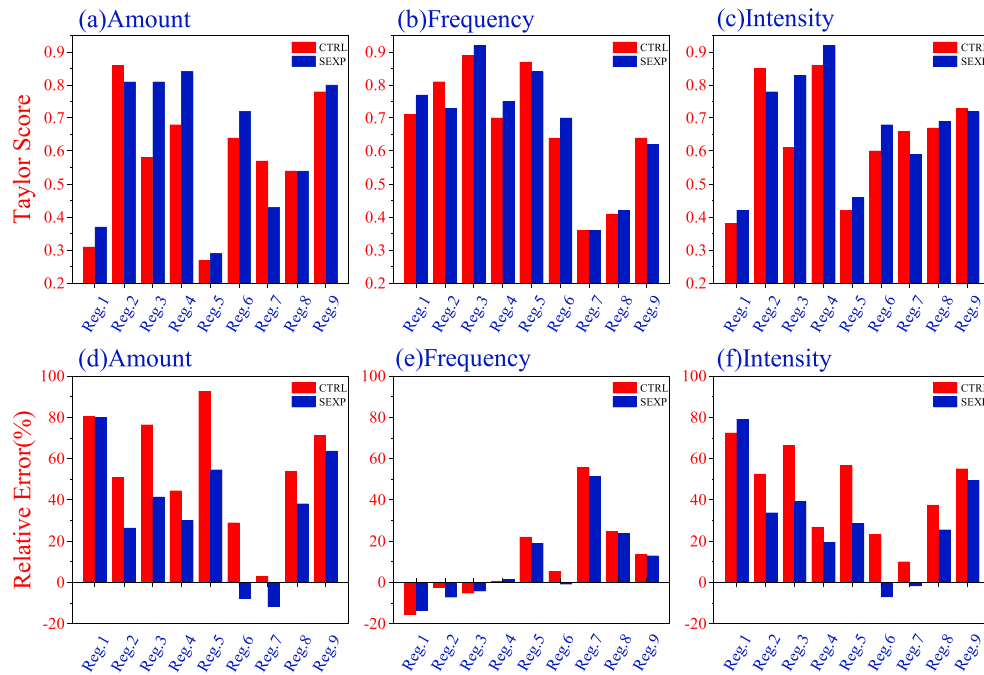


Figure 6. The Taylor scores and relative errors of the mean summer (a, d) PA, (b, e) PF, and (c, f) PI simulated by the CTRL and SEXP experiments over each subregion of China averaged over 2007–2012.

differences of regional summer mean PA for each precipitation category between the CTRL simulations and the observations, those between the SEXP simulations and observations, and those between the two experiments are shown in Figure 7. As shown in Figure 7a, the biases of total precipitation and each precipitation category in the CTRL experiment are mainly positive. The total precipitation biases in the CTRL experiment are primarily due to the biases of moderate precipitation in most subregions except southeastern China (Reg7). The bias of light or heavy precipitation is the secondary contributor to the total precipitation bias in the CTRL experiment. Figure 7 reveals that the RegCM4.1 with the STRF scheme generates smaller total PA biases in most subregions except subregions Reg1 and Reg7. The better simulated moderate and heavy precipitation, especially moderate precipitation, contributes most to the improvement of the total summer precipitation simulation over China.

Figure 8 illustrates the biases of the simulated convective precipitation (CP), large-scale precipitation (LSP), and total precipitation in the CTRL and SEXP experiments against the ERA-interim data. As shown in Figure 8a, the positive biases of the simulated CP in the SEXP experiment decrease over most subregions relative to the CTRL experiment. Figure 8b shows that the LSP produced by the CTRL experiment exhibits negative biases over most of China except subregions Reg1, Reg3, and Reg9. The simulated LSP in the SEXP experiment decreases over all subregions relative to the CTRL experiment, which increases the negative LSP biases but slightly reduces positive total precipitation biases over most of China. The fractions of CP in the total precipitation simulated by both CTRL and SEXP experiments are more than 72% over most subregions, which are higher than those of the ERA-interim data and are barely influenced by the adoption of STRF scheme (not shown). Relative to the reductions of simulated LSP, the reductions of simulated CP due to the STRF effect are also much larger. Overall, both the CP and LSP decrease due to the adoption of the STRF scheme over most regions of China. The reduction of simulated CP contributes more to the improvements of the total precipitation amount than that of the simulated LSP.

4. Possible Causes

The total surface heat exchange (HE), which includes net solar radiation flux (NSW), net long-wave radiation flux (NLW), latent heat flux (LH), and sensible heat flux (SH), can be written as $HE = NSW + NLW + LH + SH$ (Monismith & MacIntyre, 2009). Here, the positive NLW, SH, and LH are upward, while the

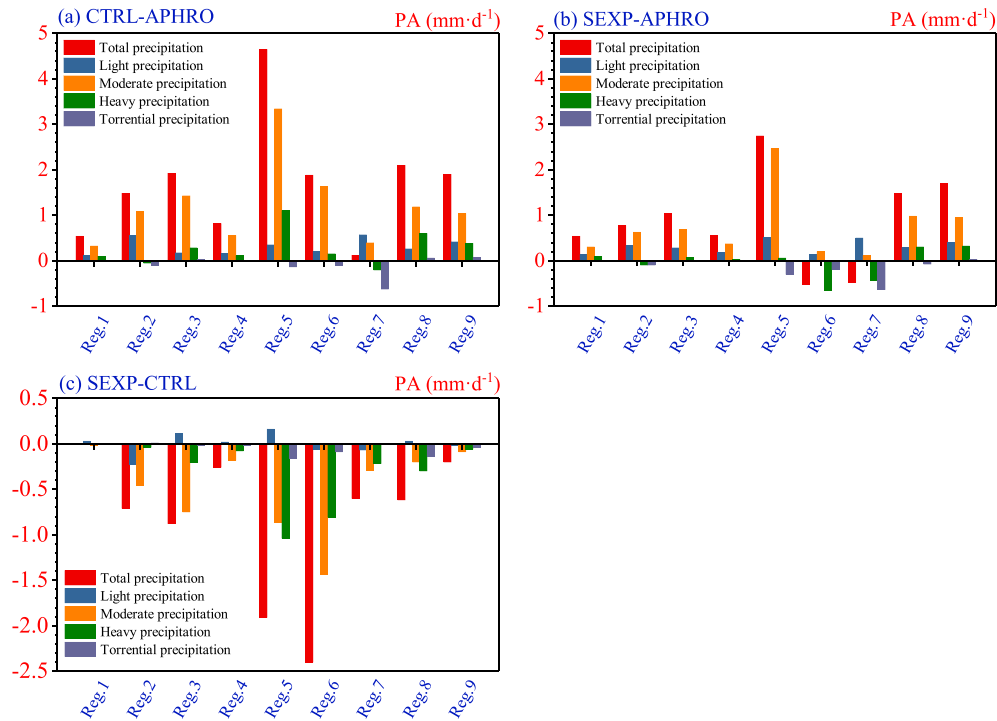


Figure 7. The differences between CTRL experiment and APHRO (CTRL – APHRO, a), between SEXP experiment and APHRO (SEXP – APHRO, b), and between CTRL experiment and SEXP experiment (SEXP – CTRL, c) in the summer mean PA of different precipitation categories over each subregion of China averaged over 2007–2012.

positive NSW is downward. The NSW+NLW is positive for the net radiation (NR) that the land surface accepts, and the SH + LH is the heat that the air column absorbs from the land surface with positive (negative) for air heating (cooling). The model differences of summer mean surface heat fluxes between the two experiments are illustrated in Figure 9. Compared to the CTRL experiment, both the NSW and NLW in the SEXP experiment decrease over the complex terrain areas. The largest NSW decrease center with the intensity of about $-40 \text{ W}\cdot\text{m}^{-2}$ is located in the southern and western flanks of the TP. Similarly, the largest NLW decrease center with the intensity of around $-15 \text{ W}\cdot\text{m}^{-2}$ is located in the southeastern and western flanks of the TP. The NSW and NLW in the SEXP experiment increase over the regions along the western Tarim Basin, part of the southwestern TP, and the northwestern Indochina Peninsula, which are associated with the decrease of simulated PF and the relatively weak local STRF. The NR differences between the CTRL and SEXP experiments are similar to that of the NSW with the maximum decreases of more than $35 \text{ W}\cdot\text{m}^{-2}$ located in the western TP flank.

As shown in Figure 9d, the SH in the SEXP experiment decreases in the northern and western TP flank, with the maximum reduction of $25 \text{ W}\cdot\text{m}^{-2}$, and increases up to $20 \text{ W}\cdot\text{m}^{-2}$ in the southeastern and southern TP flank relative to the CTRL experiment. The SH is largely determined by the near-surface thermal condition and wind speed (Dickinson et al., 1993; Elguindi et al., 2011; Yang, Guo, & Wu, 2011). Here, the SH decreases mainly due to the decrease of the ground-air temperature gradient, while the SH increases mainly because of the increased wind speed (not shown). Given that the LH is highly sensitive to precipitation, the LH in the SEXP experiment decreases in the western and southern TP flank and increases in the northern TP compared to the CTRL experiment. The decrease (increase) of the SH + LH balances with the decrease (increase) of the NR approximately over the continent. Over the complex terrain area, the land surface experiences a loss in the net radiation flux in response to the STRF. Correspondingly, less heat is transferred to the air column from the land surface.

Due to the high terrain and small total air mass over the TP, the TP can efficiently heat the middle troposphere and exert great impacts on the North Hemisphere atmospheric circulation in summer (Duan & Wu, 2005; Yang, Guo, He et al., 2011). To further illustrate the TP heat source difference between the two

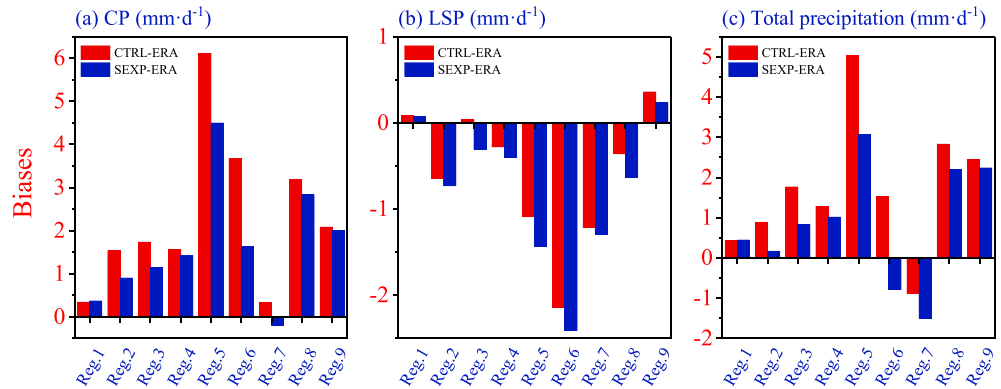


Figure 8. Model biases in the mean summer convective (a), large-scale (b), and total PA (c) over each subregion of China averaged over 2007–2012 for each experiment.

experiments, we calculate the mean surface heat fluxes over the TP (i.e., areas with the elevation over 3,000 m as marked by gray line in Figure 9). As shown in Figure 10, the regional mean surface heat fluxes over the TP in the SEXP experiment are smaller than those in the CTRL experiment. Due to the STRF effect, the TP losses $15.0 \text{ W}\cdot\text{m}^{-2}$ (11%) NR with the NSW (NLW) decreased by 20.3 (5.3) $\text{W}\cdot\text{m}^{-2}$. To balance the changes in the NR, the sum of LH and SH decreases by $14.8 \text{ W}\cdot\text{m}^{-2}$ (11%) with a reduction of 8.9 (5.9) $\text{W}\cdot\text{m}^{-2}$ for the LH (SH). Due to the weakened TP thermal forcing, less heat is released to the

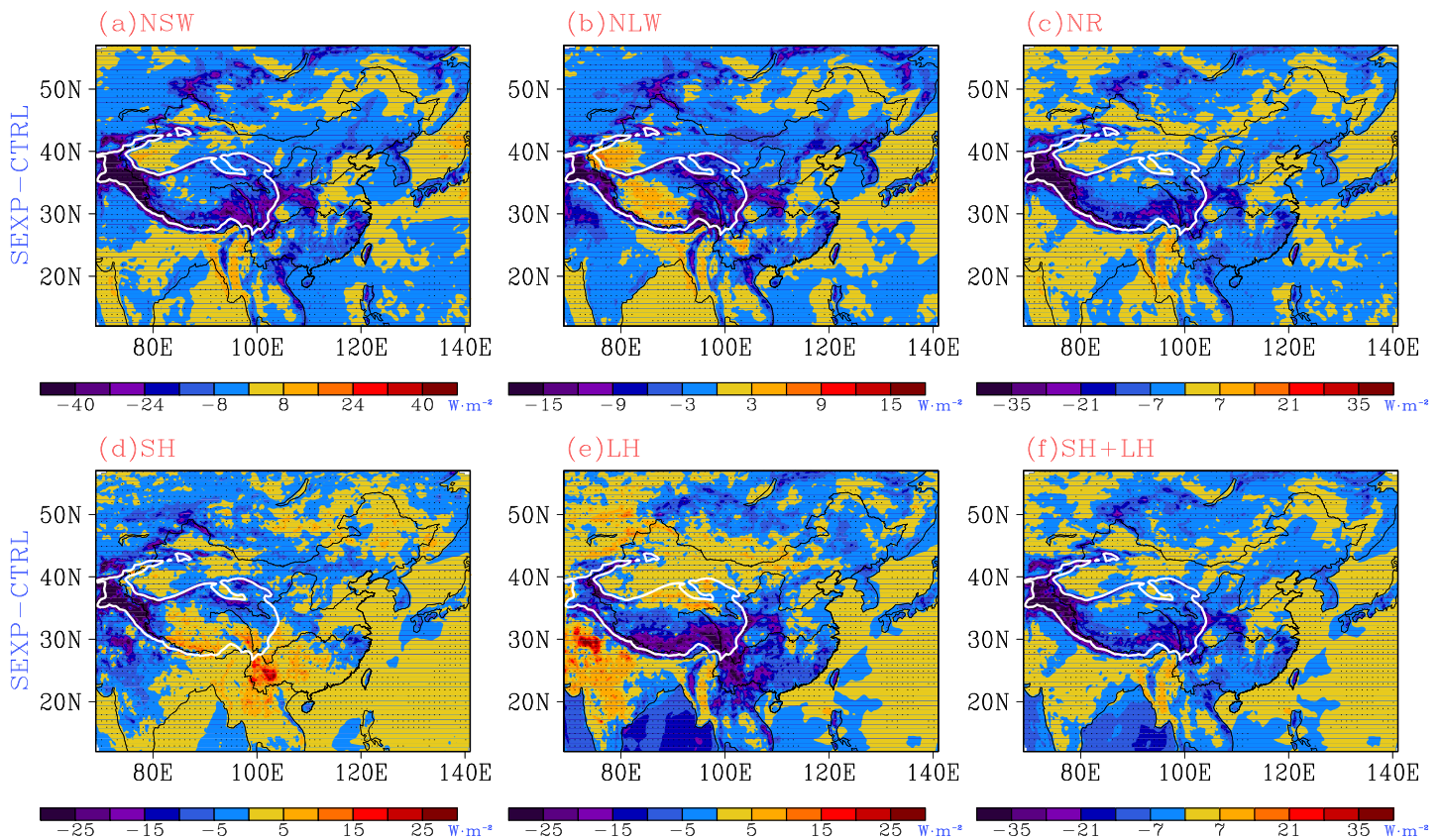


Figure 9. The differences in the summer mean surface heat fluxes averaged over 2007–2012. (a) Net solar radiation flux; (b) net long-wave radiation flux; (c) net radiation flux; (d) sensible heat flux; (e) latent heat flux; (f) sum of the sensible and latent heat fluxes. Dots indicate the differences that are significant at 95% confidence level. The gray line marks the elevation of 3,000 m. The Yangtze River and Yellow River are indicated by the dark curve lines.

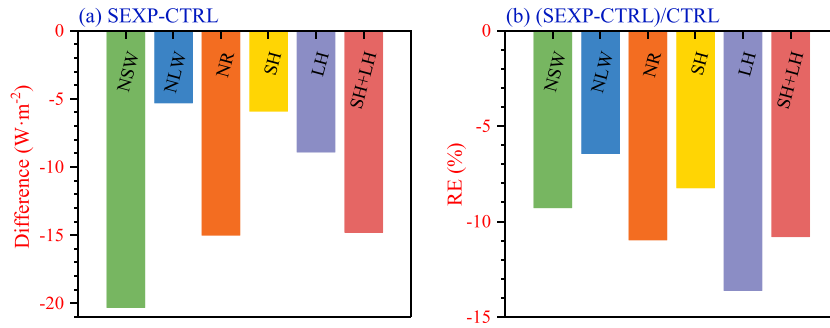


Figure 10. (a and b) The differences in the summer mean surface heat fluxes between SEXP and CTRL experiments over the area of the Tibetan Plateau with the elevation above 3,000 m averaged over 2007 – 2012.

boundary layer, which stabilizes the atmosphere, suppresses the convection locally (Rodwell & Hoskins, 1996), and further affects the climate over its surrounding regions by adjusting the atmospheric circulation.

As shown in Figure 11, the summer mean temperature averaged between 500 and 200 hPa in the CTRL experiment is cool over the ocean and warm over the land with the warm center over the north India, south of the TP (Li & Yanai, 1996). The TP has higher 500–200 hPa air temperature in the midlatitudes due to its thermal forcing. Because of the thermal adaption, the spatial distribution of the summer mean geopotential thickness (geopotential height difference between 500 and 200 hPa) resembles that of the mean temperature. Strong west (land)-east (sea) thermal contrast exists in the midlatitudes with high-pressure gradient. Due to the weakened TP thermal forcing relative to the CTRL experiment, the SEXP experiment generates a weak warm temperature anomaly (less than 0.2 K) over the western Pacific and a relatively strong cold temperature anomaly around the TP with the minimum of -0.8 K over the western TP. The difference of geopotential thickness between the two experiments is consistent with that of temperature according to the hydrostatic equilibrium assumption. The responses of temperature and geopotential thickness to the reduced TP thermal forcing are consistent with previous findings (e.g., Li & Yanai, 1996; Liu et al., 2012). In the SEXP experiment, the west (land)-east (sea) thermal contrast and pressure gradient are attenuated over the EASM region due to the terrain surface radiative forcing, indicating a weakened EASM (Chen et al., 2010; Xu et al., 2006; Yu et al., 2004).

Compared to the ERA-interim reanalysis data, the CTRL experiment reasonably reproduces the general characteristics of summer flow patterns at 850 and 200 hPa (Figures 12a–12d). The prominent wind system at 850 hPa is a vigorous low-level southwesterly jet stream, which is located over the southeast side of the TP, extends northward to 40°N and is highly connected with the water vapor transportation. At 200 hPa, the most obvious feature is the massive anticyclone (usually referred to as the South Asian High or the

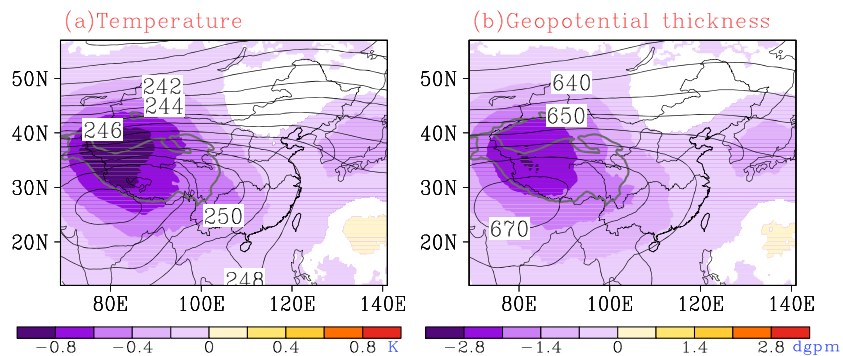


Figure 11. The summer mean (a) temperature and (b) geopotential thickness between 500 and 200 hPa averaged over 2007 – 2012. The contour plots denote the CTRL experiment results and the shadings indicate the differences between SEXP and CTRL experiments that are significant at 95% confidence level. The gray line marks the elevation of 3,000 m. The Yangtze River and Yellow River are indicated by the dark curve lines.

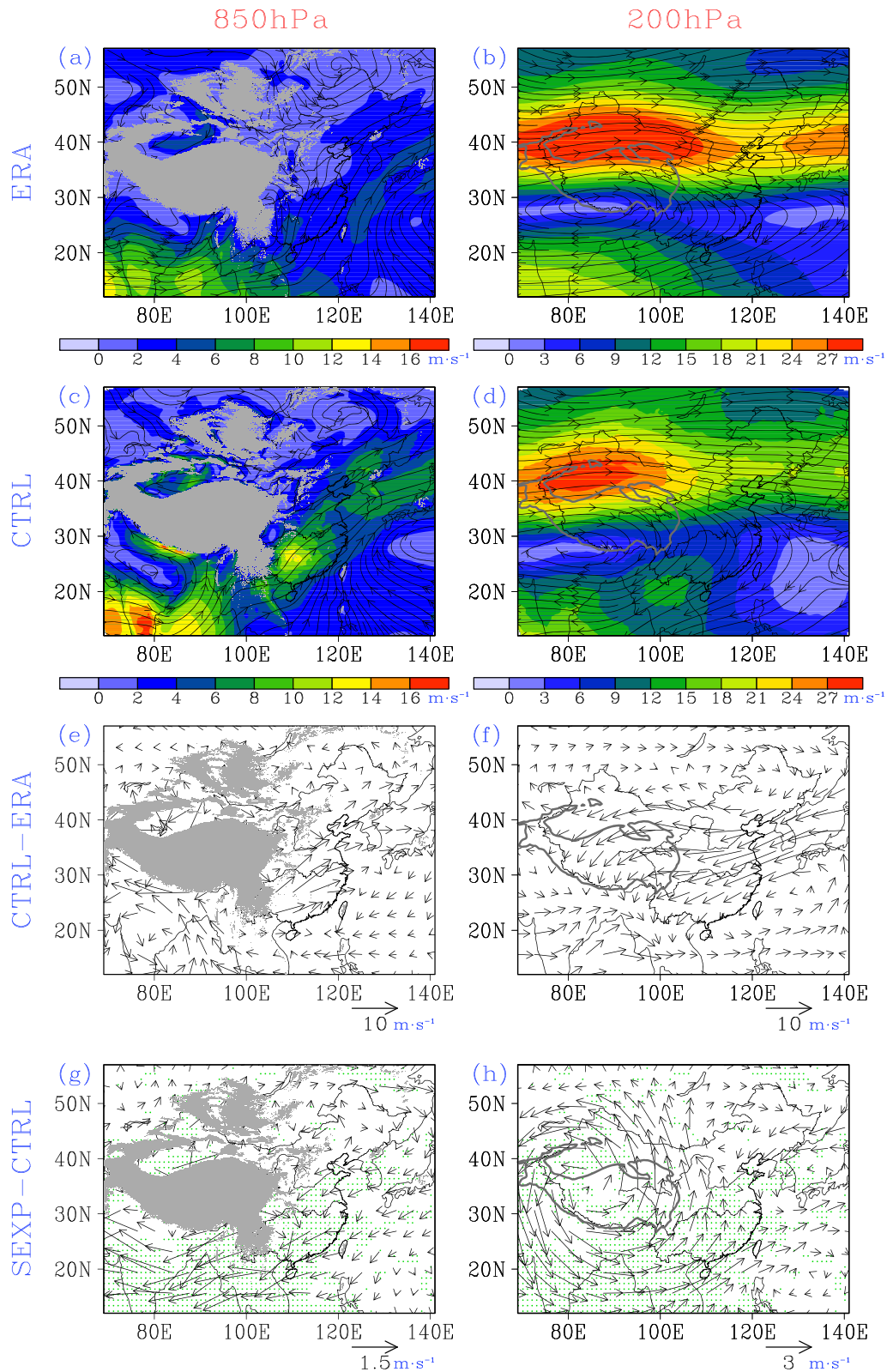


Figure 12. The summer mean wind vector at 850 hPa (left panel) and 200 hPa (right panel) averaged over 2007 – 2012 from the ERA-interim reanalysis (a, b) and the CTRL experiment (c, d). The differences of wind vector at 850 hPa (left panel) and 200 hPa (right panel) between the CTRL experiment and the ERA-interim reanalysis (CTRL – ERA, e, f), and between the two experiments (SEXP – CTRL, g, h). Dots indicate the differences that are significant at 95% confidence level. The gray line marks the elevation of 3,000 m. The Yangtze River and Yellow River are indicated by the dark curve lines.

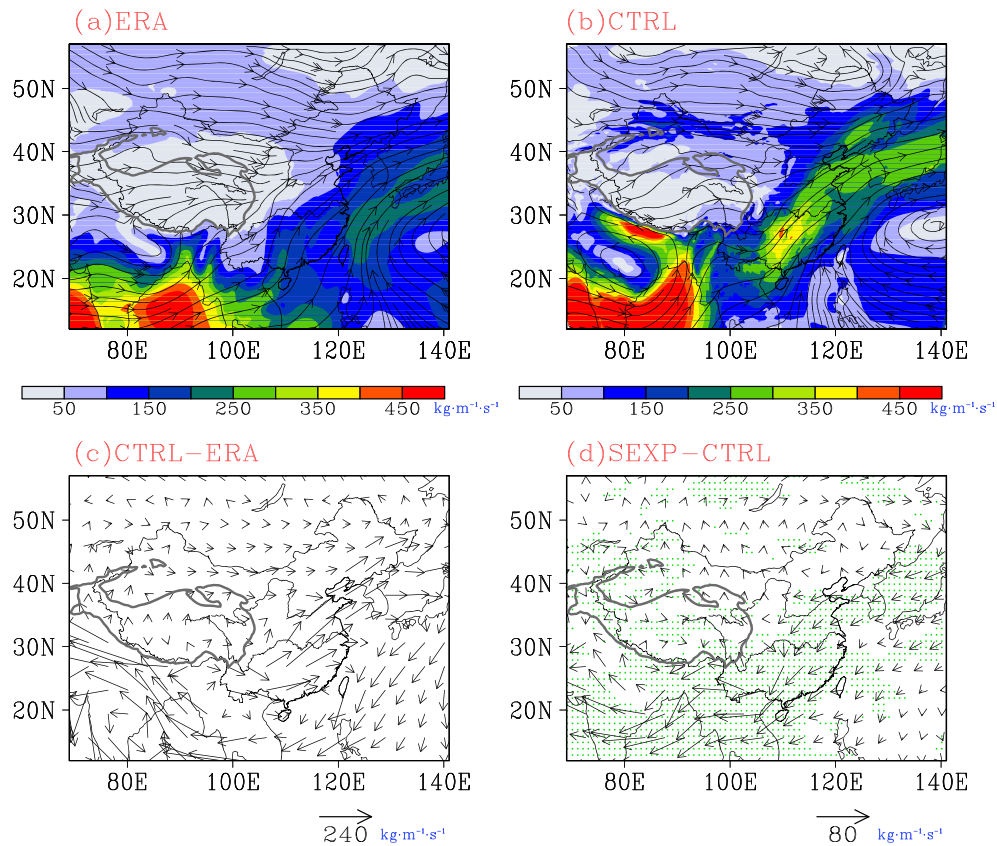


Figure 13. The summer mean water vapor transport flux vertically integrated from surface to 100 hPa averaged over 2007 – 2012 from the ERA-interim reanalysis (a) and the CTRL experiment (b). The differences of water vapor transport flux between the CTRL experiment and the ERA-interim reanalysis (CTRL – ERA, c), and between the two experiments (SEXP – CTRL, d). Dots indicate the differences that are significant at 95% confidence level. The gray line marks the elevation of 3,000 m. The Yangtze River and Yellow River are indicated by the dark curve lines.

Tibetan High), which dominates the tropics and subtropics with a center located southwest of the TP. The upper troposphere subtropical westerly jet stream is extremely important for the regional climate variations in East Asia (Yu et al., 2004). The southwesterly wind at 850 hPa and the South Asian High at 200 hPa are the consequences of the thermal adaptation to the TP thermal forcing and the important components of the EASM system (Wu et al., 2012). The CTRL experiment reproduces strong EASM with more robust southwesterly (northwesterly) wind at 850 hPa (200 hPa) over East Asia relative to those of the ERA-interim reanalysis data (Figures 12e and 12f).

As shown in Figures 12g and 12h, compared to the CTRL experiment, an anomalous northeasterly wind at 850 hPa over the southeast of the TP and a robust anomalous cyclone at 200 hPa over the TP are generated in the SEXP experiment because of the weakened TP heat source. The anomalous northeasterly wind at 850 hPa weakens the low-level southwesterly jet. The upper-level tropical easterly jet, subtropical westerly jet, and South Asian High at 200 hPa are undermined by the anomalous cyclone. These circulation anomalies are the specific features of the weakened EASM responding to the weakened TP thermal forcing, which is consistent with the previous findings (e.g., Duan et al., 2013; Liu et al., 2012; Wang et al., 2008).

One of the most essential components of the EASM system is the water vapor transportation (Duan et al., 2013; Liu et al., 2012). The vertically integrated water vapor between surface and 100 hPa in the ERA-interim reanalysis and the CTRL experiment, and the differences between the reanalysis and experiments are given in Figure 13. As shown in Figures 13a and 13b, abundant water vapor is transported from the North Indian Ocean to East Asia, which is favorable for the formation of the EASM precipitation (Duan et al., 2013). The CTRL experiment generates strong water vapor transport over East Asia relative to the ERA-interim reanalysis (Figure 13c). Figure 13d shows that the SEXP experiment simulates a relatively weaker water vapor transport corresponding to the weakened EASM. As a result, the monsoonal

rain belt is weaker in the SEXP experiment relative to the CTRL experiment (Liu et al., 1994), leading to the improved precipitation simulation over most of China (Figures 5–8).

As shown above, the RegCM4.1 with the STRF scheme generates less net surface solar and long-wave radiation fluxes over the complex terrain areas. In balance with the decreased surface net radiation flux, less heat is transported from the land to the overlying air column, which stabilizes the atmosphere and suppresses the convective precipitation locally. Meanwhile, the TP has the most unique and complex terrain in Asia, and the simulated surface heat fluxes over it are obviously affected by adopting the STRF scheme in RegCM4.1, which have impacts on the local convection, the atmospheric circulation, and the rainfall over its surrounding area. The TP surface net radiation flux simulated by the RegCM4.1 with the STRF scheme decreases by 11% and results in a weakened TP thermal forcing relative to the CTRL experiment. The weakened TP thermal forcing leads to the attenuated land-sea thermal contrast, northeastward moisture convergence belt, South Asian High, and less summer rainfall in response to the weakened EASM. The local convective rainfall suppression and the precipitation reduction related to the circulation adjustment due to the STRF improve the RegCM4.1 performance in simulating the summer precipitation over China. However, these changes due to the STRF effect in surface heat fluxes and atmospheric circulation are mainly intensity adjustments. Thus, the better simulated PAs are largely attributed to the improvements of the simulated PI with the main reduction of moderate and heavy precipitation.

5. Summary

The subgrid terrain radiative forcing scheme is introduced to the RegCM4.1 with the calibration factors \bar{u} , \bar{v} , \bar{w} , and $\cos^2(\alpha/2)$. Two experiments with and without the STRF scheme are conducted to simulate the summer climate over China during 2007 – 2012. The effects of STRF on the ability of RegCM4.1 and the possible underlying mechanisms have been investigated and revealed. The major conclusions are summarized below:

- (1) The RegCM4.1 can reproduce the general features of summer rainfall over China but exhibit positive biases over most regions of China. The STRF scheme is beneficial for the RegCM4.1 to simulate the summer precipitation over most of China except the southeastern China. The experiment with the STRF scheme obtains the largest improvements in the simulated PA over the eastern TP with a TS increased by 0.23 and a RE decrease of 35%.
- (2) Due to the adoption of STRF scheme, the improvements in the simulated PA mainly result from the improved PI simulation. In addition, the improvements in the total precipitation simulations are largely attributed to the improved moderate and heavy precipitation, and convective processes simulations.
- (3) With the adoption of STRF scheme, the RegCM4.1 generates less net radiation fluxes over the orographic land surface. Consequently, less heat is transported from the land to the air column, which stabilizes the atmosphere and suppresses the convective precipitation locally.
- (4) Relative to the CTRL experiment, the TP surface net radiation flux in the SEXP experiment with the STRF scheme decreases by 11% and results in a weakened TP thermal forcing and land-sea thermal contrast, which further leads to a weakened EASM and thereafter reduced precipitation over most of China in better agreements with the observations.

It should be noted that although the STRF scheme offers the RegCM4.1 more realistic description of surface radiation process and better precipitation simulations over complex terrain areas, it deteriorates the summer precipitation simulation over southeastern China. Therefore, further studies are needed to deeply investigate the impacts of the STRF in RegCM4.1 when performed in other regions. Additionally, long-term sensitivity experiments are necessary for identifying the performances of STRF scheme when coupling with different land surface models, cumulus convection schemes, and adopting different model resolutions. The seasonal and diurnal impacts of the STRF on the model performance should also be investigated in the future.

References

- Bartier, P. M., & Keller, C. P. (1996). Multivariate interpolation to incorporate thematic surface data using inverse distance weighting (IDW). *Computers & Geosciences*, 22(7), 795–799. [https://doi.org/10.1016/0098-3004\(96\)00021-0](https://doi.org/10.1016/0098-3004(96)00021-0)

Acknowledgments

This study is supported by the National Key R&D Program of China under Grant 2017YFA0604301, National Natural Science Foundation of China under Grants 41975081 and 41975130, the Jiangsu University “Blue Project” outstanding young teachers training object, the Fundamental Research Funds for the Central Universities, and the Jiangsu Collaborative Innovation Center for Climate Change. We appreciate ICTP for releasing the codes of RegCM4.1, which are available at the website (<http://gforge.ictp.it/gf/project/regcm/>). We are also grateful to CIAT (<http://srtm.csi.cgiar.org>), USGS (<https://www.usgs.gov>), NCEP (<https://www.esrl.noaa.gov/psd/data/gridded/data.ncep.reanalysis.html>), NOAA (<https://www.esrl.noaa.gov/psd/data/gridded/data.noaa.oisst.v2.html>), MRI/JMA (<http://aphrodite.st.hirosaki-u.ac.jp>), and ECMWF (<https://www.ecmwf.int>) for allowing us to use the data. We show our gratitude and respect to the three anonymous reviewers for their constructive and insightful suggestions to greatly help improve the manuscript.

- Boo, K. O., Martin, G., Sellar, A., Senior, C., & Byun, Y. H. (2011). Evaluating the East Asian monsoon simulation in climate models. *Journal of Geophysical Research*, *116*, D01109. <https://doi.org/10.1029/2010JD014737>
- Caldwell, P., Chin, H.-N. S., Bader, D. C., & Bala, G. (2009). Evaluation of a WRF dynamical downscaling simulation over California. *Climatic Change*, *95*(3-4), 499–521. <https://doi.org/10.1007/s10584-009-9583-5>
- Chang, E. C., Yeh, S. W., Hong, S. Y., & Wu, R. (2013). Sensitivity of summer precipitation to tropical sea surface temperatures over East Asia in the GRIMs GMP. *Geophysical Research Letters*, *40*, 1824–1831. <https://doi.org/10.1002/grl.50389>
- Chen, B., Chao, W. C., & Liu, X. (2003). Enhanced climatic warming in the Tibetan Plateau due to doubling CO₂: A model study. *Climate Dynamics*, *20*(4), 433–413. <https://doi.org/10.1007/s00382-003-0308-6>
- Chen, B., Zhang, Y. C., & Ding, Y. G. (2006). The effect of terrain fluctuation on the computed surface long-wave radiation in the models (Chinese with English abstract). *Plateau Meteorology*, *25*(3), 406–412. <https://doi.org/10.3321/j.issn:1000-0534.2006.03.007>
- Chen, H., Zhou, T., Neale, R. B., Wu, X., & Zhang, G. J. (2010). Performance of the new NCAR CAM3.5 model in East Asian summer monsoon simulations: Sensitivity to modifications of the convection scheme. *Journal of Climate*, *23*(13), 3657–3675. <https://doi.org/10.1175/2010jcli3022.1>
- Chen, J., Yin, Y., Chen, Q., Ding, H., & Xiao, H. (2014). Effect of convection schemes on the simulation of monsoon climates: A sensitivity study using RegCM4. *Climate Research*, *60*(2), 147–162. <https://doi.org/10.3354/cr01229>
- Chen, Y., Hall, A., & Liou, K. N. (2006). Application of three-dimensional solar radiative transfer to mountains. *Journal of Geophysical Research*, *111*, D21111. <https://doi.org/10.1029/2006JD007163>
- Chiang, J. C. H., Wu, C. H., & Kong, W. (2016). Origins of East Asian summer monsoon seasonality. Paper presented at the AGU Fall Meeting Abstracts
- Dee, D. P., Uppala, S. M., Simmons, A. J., Berrisford, P., Poli, P., Kobayashi, S., et al. (2011). The ERA-interim reanalysis: Configuration and performance of the data assimilation system. *Quarterly Journal of the Royal Meteorological Society*, *137*(656), 553–597. <https://doi.org/10.1002/qj.828>
- Dickinson, R. E., Henderson-Sellers, A., & Kennedy, P. J. (1993). Biosphere-Atmosphere Transfer Scheme (BATS) version 1e as coupled to the NCAR community climate model. Technical note. [NCAR (National Center for Atmospheric Research)]. Paper presented at the NCAR Tech Note. <https://doi.org/10.5065/D67W6959>
- Ding, Y., & Chan, J. C. L. (2005). The East Asian summer monsoon: An overview. *Meteorology and Atmospheric Physics*, *89*, 117–142. <https://doi.org/10.1007/s00703-005-0125-z>
- Dozier, J., & Outcalt, S. I. (1979). An approach toward energy balance simulation over rugged terrain. *Geographical Analysis*, *11*(1), 65–85. <https://doi.org/10.1111/j.1538-4632.1979.tb00673.x>
- Duan, A., Wang, M., Lei, Y., & Cui, Y. (2013). Trends in summer rainfall over China associated with the Tibetan Plateau sensible heat source during 1980–2008. *Journal of Climate*, *26*(1), 261–275. <https://doi.org/10.1175/jcli-d-11-00669.1>
- Duan, A. M., & Wu, G. X. (2005). Role of the Tibetan Plateau thermal forcing in the summer climate patterns over subtropical Asia. *Climate Dynamics*, *24*(7–8), 793–807. <https://doi.org/10.1007/s00382-004-0488-8>
- Dubayah, R., Dozier, J., & Davis, F. W. (1990). Topographic distribution of clear-sky radiation over the Konza prairie, Kansas. *Water Resources Research*, *26*(4), 679–690. <https://doi.org/10.1029/WR026i004p00679>
- Elguindi, N., Bi, X., Giorgi, F., Nagarajan, B., Pal, J., Solmon, F., et al. (2011). *Regional climatic model RegCM user manual version 4.1*. Strada Costiera, Trieste: The Abdus Salam International Centre for Theoretical Physics.
- Essery, R., & Marks, D. (2007). Scaling and parametrization of clear-sky solar radiation over complex topography. *Journal of Geophysical Research*, *112*, D10122. <https://doi.org/10.1029/2006JD007650>
- Feser, F., Rockel, B., von Storch, H., Winterfeldt, J., & Zahn, M. (2011). Regional climate models add value to global model data: A review and selected examples. *Bulletin of the American Meteorological Society*, *92*(9), 1181–1192. <https://doi.org/10.1175/2011BAMS3061.1>
- Flohn, H. (1957). Large-scale aspects of the “summer monsoon” in south and East Asia. *Journal of the Meteorological Society of Japan*, *35*, 180–186. https://doi.org/10.2151/jmsj1923.35a_0_180
- Fritsch, J. M., & Chappell, C. F. (1980). Numerical prediction of convectively driven mesoscale pressure systems. Part I: Convective parameterization. *Journal of the Atmospheric Sciences*, *37*(8), 1722–1733. [https://doi.org/10.1175/1520-0469\(1980\)037<1734:NPOCDM>2.0.CO;2](https://doi.org/10.1175/1520-0469(1980)037<1734:NPOCDM>2.0.CO;2)
- Fu, B. P. (1958). Effects of sloping fields on sunshine and solar radiation (Chinese). *Journal of Nanjing University (Nature Science Edition)*, *2*, 25–48.
- Fu, B. P. (1983). *Climate in mountainous regions (Chinese)* (pp. 3–10). Beijing: Science Press.
- Fu, C., Wang, S., Xiong, Z., Gutowski, W. J., Lee, D. -K., McGregor, J. L., et al. (2005). Regional climate model intercomparison project for Asia. *Bulletin of the American Meteorological Society*, *86*(2), 257–266. <https://doi.org/10.1175/BAMS-86-2-257>
- Gao, X., Shi, Y., & Giorgi, F. (2016). Comparison of convective parameterizations in RegCM4 experiments over China with CLM as the land surface model. *Atmospheric and Oceanic Science Letters*, *9*(4), 246–254. <https://doi.org/10.1080/16742834.2016.1172938>
- Gao, X., Xu, Y., Zhao, Z., Pal, J., & Giorgi, F. (2006). On the role of resolution and topography in the simulation of East Asia precipitation. *Theoretical and Applied Climatology*, *86*, 173–185. <https://doi.org/10.1007/s00704-005-0214-4>
- Garnier, B. J., & Ohmura, A. (1968). A method of calculating the direct shortwave radiation income of slopes. *Journal of Applied Meteorology*, *7*(5), 796–800. [https://doi.org/10.1175/1520-0450\(1968\)007<0796:AMOCTD>2%2E0%2ECO%3B2](https://doi.org/10.1175/1520-0450(1968)007<0796:AMOCTD>2%2E0%2ECO%3B2)
- Giorgi, F., Jones, C., & Asrar, G. R. (2009). Addressing climate information needs at the regional level: The CORDEX framework. *World Meteorological Organization (WMO) Bulletin*, *58*(3), 175–183.
- Giorgi, F., Pal, J., Bi, X., Sloan, L., Elguindi, N., & Solmon, F. (2006). Introduction to the TAC special issue: The RegCNET network. *Theoretical and Applied Climatology*, *86*(1–4), 1–4. <https://doi.org/10.1007/s00704-005-0199-z>
- Grell, G. (1993). Prognostic evaluation of assumptions used by cumulus parameterizations. *Monthly Weather Review*, *121*(3), 764–787. [https://doi.org/10.1175/1520-0493\(1993\)121<0764:PEOAU>2.0.CO;2](https://doi.org/10.1175/1520-0493(1993)121<0764:PEOAU>2.0.CO;2)
- Gu, C. L., Fang, D. X., Zhou, Y., & Huang, A. N. (2018). Effects of subgrid-scale orographic radiation parameterization on RegCM4.1's performance in simulating the climate over East Asia in summer (Chinese with English abstract). *Journal of the Meteorological Sciences*, *38*, 585–595. <https://doi.org/10.3969/2018jms.0014>
- Gu, Y., Liou, K. N., Lee, W. L., & Leung, L. R. (2012). Simulating 3D radiative transfer effects over the Sierra Nevada Mountains using WRF. *Atmospheric Chemistry and Physics Discussions*, *12*(20), 9965–9976. <https://doi.org/10.5194/acp-12-9965-2012>
- Hauge, G., & Hole, L. R. (2003). Implementation of slope irradiance in Mesoscale model version 5 and its effect on temperature and wind fields during the breakup of a temperature inversion. *Journal of Geophysical Research*, *108*(D2), 4058. <https://doi.org/10.1029/2002JD002575>

- Holtzlag, A. A. M., de Bruijn, E. I. F., & Pan, H. L. (1990). A high resolution air mass transformation model for shortrange weather forecasting. *Monthly Weather Review*, *118*(8), 1561–1575. [https://doi.org/10.1175/1520-0493\(1990\)118<1561:AHRAMT>2.0.CO;2](https://doi.org/10.1175/1520-0493(1990)118<1561:AHRAMT>2.0.CO;2)
- Huang, A., Zhao, Y., Zhou, Y., Yang, B., Zhang, L., Dong, X., et al. (2016). Evaluation of multisatellite precipitation products by use of ground based data over China. *Journal of Geophysical Research: Atmospheres*, *121*, 10,654–10,675. <https://doi.org/10.1002/2016JD025456>
- Huang, D. Q., Zhu, J., Zhang, Y. C., Huang, Y., & Kuang, X. Y. (2016). Assessment of summer monsoon precipitation derived from five reanalysis datasets over East Asia. *Quarterly Journal of the Royal Meteorological Society*, *142*(694), 108–119. <https://doi.org/10.1002/qj.2634>
- Jain, S., Mishra, S. K., Salunke, P., & Sahany, S. (2019). Importance of the resolution of surface topography vis-à-vis atmospheric and surface processes in the simulation of the climate of Himalaya-Tibet highland. *Climate Dynamics*, *52*(7-8), 4735–4748. <https://doi.org/10.1007/s00382-018-4411-0>
- Jarvis, A., Reuter, H. I., Nelson, A., & Guevara, E. (2008). *Hole-filled SRTM for the globe version 4*. International Centre for Tropical Agriculture (CIAT). Available from the CGIAR-CSI SRTM 90m Database. <http://srtm.csi.cgiar.org>
- Kalnay, E., Kanamitsu, M., Kistler, R., Collins, W., Deaven, D., Gandin, L., et al. (1996). The NCEP/NCAR 40-year reanalysis project. *Bulletin of the American Meteorological Society*, *77*(3), 437–471. [https://doi.org/10.1175/1520-0477\(1996\)077<0437:TNYRP>2.0.CO;2](https://doi.org/10.1175/1520-0477(1996)077<0437:TNYRP>2.0.CO;2)
- Kan, M. Y., Huang, A. N., Zhao, Y., Zhou, Y., Yang, B., & Wu, H. (2015). Evaluation of the summer precipitation over China simulated by BCC_CSM model with different horizontal resolutions during the recent half century. *Journal of Geophysical Research: Atmospheres*, *120*, 4657–4670. <https://doi.org/10.1002/2015JD023131>
- Kang, S., Im, E., & Ahn, J. (2014). The impact of two land-surface schemes on the characteristics of summer precipitation over East Asia from the RegCM4 simulations. *International Journal of Climatology*, *34*, 3986–3997. <https://doi.org/10.1002/joc.3998>
- Kitoh, A. (2004). Effects of mountain uplift on East Asian summer climate investigated by a coupled atmosphere-ocean GCM. *Journal of Climate*, *17*(4), 783–802. [https://doi.org/10.1175/1520-0442\(2004\)017<0783:EOMUOE>2.0.CO;2](https://doi.org/10.1175/1520-0442(2004)017<0783:EOMUOE>2.0.CO;2)
- Kosaka, Y., Xie, S. P., & Nakamura, H. (2011). Dynamics of interannual variability in summer precipitation over East Asia. *Journal of Climate*, *24*(20), 5435–5453. <https://doi.org/10.1175/2011jcli4099.1>
- Lee, W. L., Gu, Y., Liou, K. N., Leung, L. R., & Hsu, H. H. (2015). A global model simulation for 3-D radiative transfer impact on surface hydrology over the Sierra Nevada and Rocky Mountains. *Atmospheric Chemistry and Physics*, *15*, 5405–5413. <https://doi.org/10.5194/acp-15-5405-2015>
- Lee, W. L., Liou, K. N., & Hall, A. (2011). Parameterization of solar fluxes over mountain surfaces for application to climate models. *Journal of Geophysical Research*, *116*, D01101. <https://doi.org/10.1029/2010JD014722>
- Li, C. F., & Yanai, M. (1996). The onset and interannual variability of the Asian summer monsoon in relation to land-sea thermal contrast. *Journal of Climate*, *9*(2), 358–375. [https://doi.org/10.1175/1520-0442\(1996\)009<0358:TOAIVO>2.0.CO;2](https://doi.org/10.1175/1520-0442(1996)009<0358:TOAIVO>2.0.CO;2)
- Li, W. P., Wu, G. X., Liu, Y. M., & Liu, Y. (2001). How the surface processes over the Tibetan Plateau affect the summertime Tibetan anticyclone: Numerical experiments (Chinese with English abstract). *Chinese Journal of Atmospheric Sciences*, *25*(6), 809–816. <https://doi.org/10.3878/j.jissn.1006-9895.2001.06.08>
- Li, X., Chen, X. Z., & Zeng, Q. Z. (1996). A model to calculate the net solar radiation over complex terrain based on digital terrain model (Chinese with English abstract). *Journal of Glaciology and Geocryology*, *18*(S1), 344–353.
- Li, Z. Q., & Weng, D. M. (1987). A computer model to determine topographic parameters (Chinese with English abstract). *Acta Geographica Sinica*, *54*(3), 269–278. <https://doi.org/10.11821/xb198703009>
- Lin, R., Zhou, T., & Qian, Y. (2014). Evaluation of global monsoon precipitation changes based on five reanalysis datasets. *Journal of Climate*, *27*(3), 1271–1289. <https://doi.org/10.1175/JCLI-D-13-00215.1>
- Liou, K. N., Lee, W. L., & Hall, A. (2007). Radiative transfer in mountains: Application to the Tibetan Plateau. *Geophysical Research Letters*, *34*, L23809. <https://doi.org/10.1029/2007GL031762>
- Liu, X. P., Wang, H. J., He, M. Y., & Shi, X. K. (2013). Influence of land surface schemes on precipitation simulation (Chinese with English abstract). *Advances in Water Science*, *24*(5), 658–666.
- Liu, Y., Giorgi, F., & Washington, W. M. (1994). Simulation of summer monsoon climate over East Asia with an NCAR regional climate model. *Monthly Weather Review*, *122*(10), 2331–2348. [https://doi.org/10.1175/1520-0493\(1994\)122<2331:SOSMCO>2.0.CO;2](https://doi.org/10.1175/1520-0493(1994)122<2331:SOSMCO>2.0.CO;2)
- Liu, Y., Wu, G., Hong, J., Dong, B., Duan, A., Bao, Q., & Zhou, L. (2012). Revisiting Asian monsoon formation and change associated with Tibetan Plateau forcing: II. *Change. Climate Dynamics*, *39*(5), 1183–1195. <https://doi.org/10.1007/s00382-012-1335-y>
- Monismith, S. G., & MacIntyre, S. (2009). The surface mixed layer in lakes and reservoirs. In *Biogeochemistry of inland waters* (pp. 207–221). San Diego: Elsevier.
- Moore, G. W. K. (2012). Surface pressure record of Tibetan Plateau warming since the 1870s. *Quarterly Journal of the Royal Meteorological Society*, *138*(669), 1999–2008. <https://doi.org/10.1002/qj.1948>
- Müller, M. D., & Scherer, D. (2005). A grid- and subgrid-scale radiation parameterization of topographic effects for mesoscale weather forecast models. *Monthly Weather Review*, *133*(6), 1431–1442. <https://doi.org/10.1175/MWR2927.1>
- Pal, J. S., Small, E. E., & Eltahir, E. A. B. (2000). Simulation of regional-scale water and energy budgets: Representation of subgrid cloud and precipitation processes within RegCM. *Journal of Geophysical Research*, *105*(D24), 29,579–29,594. <https://doi.org/10.1029/2000JD900415>
- Pierce, D. W., Cayan, D. R., Das, T., Maurer, E. P., Miller, N. L., Bao, Y., et al. (2013). The key role of heavy precipitation events in climate model disagreements of future annual precipitation changes in California. *Journal of Climate*, *26*(16), 5879–5896. <https://doi.org/10.1175/jcli-d-12-00766.1>
- Qian, Y., & Leung, L. R. (2007). A long-term regional simulation and observations of the hydroclimate in China. *Journal of Geophysical Research*, *112*, D14104. <https://doi.org/10.1029/2006JD008134>
- Qiao, L., Li, Y. X., Fu, J. L., Tian, C. Y., Bi, B. G., & Zhou, Q. L. (2012). *National standards of the People's Republic of China: Grade of precipitation GB/T 28592-2012 (Chinese)*. Beijing: Standards Press of China.
- Reynolds, R. W., Banzon, V. F., & NOAA CDR Program (2008). *NOAA Optimum Interpolation 1/4 Degree Daily Sea Surface Temperature (OISST) analysis, version 2*. NOAA National Centers for Environmental Information. <https://doi.org/10.7289/V5SQ8XB5>
- Rodwell, M. J., & Hoskins, B. J. (1996). Monsoons and the dynamics of deserts. *Quarterly Journal of the Royal Meteorological Society*, *122*(534), 1385–1404. <https://doi.org/10.1002/qj.49712253408>
- Ruiz-Arias, J. A., Pozo-Vázquez, D., Lara-Fanego, V., Santos-Alamillos, F. J., & Tovar-Pescador, J. (2011). A high-resolution topographic correction method for clear-sky solar irradiance derived with a numerical weather prediction model. *Journal of Applied Meteorology and Climatology*, *50*, 2460–2472. <https://doi.org/10.1175/2011JAMC2571.1>
- Senkova, A. V., Rontu, L., & Savijärvi, H. (2007). Parametrization of orographic effects on surface radiation in HIRLAM. *Tellus A: Dynamic Meteorology and Oceanography*, *59*(3), 279–291. <https://doi.org/10.1111/j.1600-0870.2007.00235.x>

- Shen, Y., & Hu, J. (2006). Slope irradiance scheme in GRAPES and its effect on simulation of short-range weather processes (Chinese with English abstract). *Chinese Journal of Atmospheric Sciences*, 30(6), 75–83. <https://doi.org/10.3878/j.issn.1006-9895.2006.06.07>
- Solomon, S., Qin, D., Manning, M., & Chen, Z. (2007). *Climate change 2007: The physical science basis: Working group I contribution to the fourth assessment report of the IPCC* (Vol. 4). New York: Cambridge University Press.
- Stocker, T. (2014). *Climate change 2013: The physical science basis: Working Group I contribution to the Fifth Assessment Report of the Intergovernmental Panel on Climate Change*. New York: Cambridge University Press.
- Taylor, K. E. (2001). Summarizing multiple aspects of model performance in a single diagram. *Journal of Geophysical Research*, 106(D7), 7183–7192. <https://doi.org/10.1029/2000JD900719>
- Torma, C., Giorgi, F., & Coppola, E. (2015). Added value of regional climate modeling over areas characterized by complex terrain-precipitation over the Alps. *Journal of Geophysical Research: Atmospheres*, 120, 3957–3972. <https://doi.org/10.1002/2014JD022781>
- Vardavas, I. M., & Taylor, F. W. (2011). *Radiation and climate: Atmospheric energy budget from satellite remote sensing*. New York: Oxford University Press.
- Wang, B., Bao, Q., Hoskins, B., Wu, G., & Liu, Y. (2008). Tibetan Plateau warming and precipitation changes in East Asia. *Geophysical Research Letters*, 35, L14702. <https://doi.org/10.1029/2008GL034330>
- Wang, K. C., Zhou, X. J., & Liu, J. M. (2004). The effects of complex terrain on the computed surface solar short-wave radiation (Chinese with English abstract). *Chinese Journal of Atmospheric Sciences*, 28(4), 625–633. <https://doi.org/10.3878/j.issn.1006-9895.2004.04.14>
- Weng, D. M., Chen, W. L., Shen, J. C., & Gao, J. B. (1981). *Microclimate and agricultural microclimate* (Chinese) (pp. 5–11). Beijing: Agriculture Press.
- Whiteman, C. D., Allwine, K. J., Fritschen, L. J., Orgill, M. M., & Simpson, J. R. (1989). Deep valley radiation and surface energy budget microclimates. Part I: Radiation. *Journal of Applied Meteorology*, 28(6), 414–426. [https://doi.org/10.1175/1520-0450\(1989\)028<0414:DVRASE>2.0.CO;2](https://doi.org/10.1175/1520-0450(1989)028<0414:DVRASE>2.0.CO;2)
- Wu, G. X., Liu, Y. M., Dong, B. W., Liang, X. Y., Duan, A., Bao, Q., & Yu, J. J. (2012). Revisiting Asian monsoon formation and change associated with Tibetan Plateau forcing: I. Formation. *Climate Dynamics*, 39(5), 1169–1181. <https://doi.org/10.1007/s00382-012-1334-z>
- Wu, G., Liu, Y., Zhang, Q., Duan, A., Wang, T., Wan, R., et al. (2007). The influence of mechanical and thermal forcing by the Tibetan Plateau on Asian climate. *Journal of Hydrometeorology*, 8(4), 770–789. <https://doi.org/10.1175/JHM609.1>
- Wu, H. M., Huang, A. N., Zhou, Y., & Zhang, L. (2015). Evaluation of the performance of RegCM4.1 in simulating climate over China (Chinese with English abstract). *Journal of the Meteorological Sciences*, 35(1), 17–25. <https://doi.org/10.3969/2013jms.0049>
- Xu, J., Koldunov, N., Remedio, A. R. C., Sein, D. V., Zhi, X., Jiang, X., et al. (2018). On the role of horizontal resolution over the Tibetan Plateau in the REMO regional climate model. *Climate Dynamics*, 51(11-12), 4525–4542. <https://doi.org/10.1007/s00382-018-4085-7>
- Xu, M., Chang, C. P., Fu, C. B., Qi, Y., Robock, A., Robinson, D., & Zhang, H.-M. (2006). Steady decline of East Asian monsoon winds, 1969–2000: Evidence from direct ground measurements of wind speed. *Journal of Geophysical Research*, 111, D24111. <https://doi.org/10.1029/2006JD007337>
- Xu, Y., & Xu, C. (2012). Preliminary assessment of simulations of climate changes over China by CMIP5 multi-models. *Atmospheric Oceanic Science Letters*, 5(6), 489–494. <https://doi.org/10.1080/16742834.2012.11447041>
- Yanai, M., & Wu, G. X. (2006). Role of the Tibetan Plateau on Asia monsoon. In B. Wang (Ed.), *The Asian monsoon* (pp. 513–629). Berlin: Springer.
- Yang, B., Zhang, Y., Qian, Y., Huang, A., & Yan, H. (2015). Calibration of a convective parameterization scheme in the WRF model and its impact on the simulation of East Asian summer monsoon precipitation. *Climate Dynamics*, 44(5–6), 1661–1684. <https://doi.org/10.1007/s00382-014-2118-4>
- Yang, K., Guo, X., He, J., Qin, J., & Koike, T. (2011). On the climatology and trend of the atmospheric heat source over the Tibetan Plateau: An experiments-supported revisit. *Journal of Climate*, 24(5), 1525–1541. <https://doi.org/10.1175/2010JCLI3848.1>
- Yang, K., Guo, X., & Wu, B. (2011). Recent trends in surface sensible heat flux on the Tibetan Plateau. *Science China Earth Sciences*, 54(1), 19–28. <https://doi.org/10.1007/s11430-010-4036-6>
- Yatagai, A., Kamiguchi, K., Arakawa, O., Hamada, A., Yasutomi, N., & Kitoh, A. (2012). APHRODITE: Constructing a long-term daily gridded precipitation dataset for Asia based on a dense network of rain gauges. *Bulletin of the American Meteorological Society*, 93(9), 1401–1415. <https://doi.org/10.1175/BAMS-D-11-00122.1>
- Yeh, T. C., Luo, S. W., & Chu, P. C. (1957). The wind structure and heat balance in the lower troposphere over Tibetan Plateau and its surrounding (Chinese with English abstract). *Acta Meteorologica Sinica*, 28(2), 108–121. <https://doi.org/10.11676/qxxb1957.010>
- Yhang, Y. B., & Hong, S. Y. (2008). Improved physical processes in a regional climate model and their impact on the simulated summer monsoon circulations over East Asia. *Journal of Climate*, 21(5), 963–979. <https://doi.org/10.1175/2007jcli1694.1>
- Yu, R., Wang, B., & Zhou, T. (2004). Tropospheric cooling and summer monsoon weakening trend over East Asia. *Geophysical Research Letters*, 31, L22212. <https://doi.org/10.1029/2004GL021270>
- Yu, Y., & Xie, Z. H. (2013). A simulation study on climatic effects of land cover change in China. *Advances in Climate Change Research*, 4(2), 117–126. <https://doi.org/10.3724/SP.J.1248.2013.117>
- Zeng, X., Zhao, M., & Dickinson, R. E. (1998). Intercomparison of bulk aerodynamic algorithms for the computation of sea surface fluxes using TOGA COARE and TAO data. *Journal of Climate*, 11(10), 2628–2644. [https://doi.org/10.1175/1520-0442\(1998\)011<2628:IOBAAF>2.0.CO;2](https://doi.org/10.1175/1520-0442(1998)011<2628:IOBAAF>2.0.CO;2)
- Zhang, Y. C., Ding, Y. G., & Chen, B. (2006). The influence of orographic heterogeneity on parameterization of regional mean long-wave radiation flux (Chinese with English abstract). *Acta Meteorologica Sinica*, 64(1), 39–47. <https://doi.org/10.11676/qxxb2006.004>
- Zhang, Y. C., Huang, A. N., & Zhu, X. S. (2006). Parameterization of the thermal impacts of sub-grid orography on numerical modeling of the surface energy budget over East Asia. *Theoretical and Applied Climatology*, 86(1-4), 201–214. <https://doi.org/10.1007/s00704-005-0209-1>
- Zhong, Z., Hu, Y. J., Min, J. Z., & Xu, H. L. (2007). Numerical experiments on the spin-up time for seasonal-scale regional climate modeling. *Journal of Meteorological Research*, 21(4), 409–419.
- Zhou, T., Yu, R., Chen, H., Dai, A., & Pan, Y. (2008). Summer precipitation frequency, intensity, and diurnal cycle over China: A comparison of satellite data with rain gauge observations. *Journal of Climate*, 21, 3997–4010. <https://doi.org/10.1175/2008JCLI2028.1>
- Zou, L., & Zhou, T. (2011). Sensitivity of a regional ocean-atmosphere coupled model to convection parameterization over western North Pacific. *Journal of Geophysical Research*, 116, D18106. <https://doi.org/10.1029/2011JD015844>
- Zou, L., Zhou, T., Laurent, L., & Zhang, J. (2010). East China summer rainfall variability of 1958–2000: Dynamical downscaling with a variable resolution AGCM. *Journal of Climate*, 23, 6394–6408. <https://doi.org/10.1175/2010JCLI3689.1>